

Numerical Methods for Hypersonic Boundary Layer Stability

M. R. MALIK

*High Technology Corporation, P.O. Box 7262,
Hampton, Virginia 23666*

Received July 26, 1988; revised March 22, 1989

Various numerical methods for the solution of linear stability equations for compressible boundary layers are compared. Both the global and local eigenvalue methods for temporal stability analysis are discussed. Global methods are used to compute all the eigenvalues of the discretized system. When a guess for the desired eigenvalue is available, local methods may be used both to purify the eigenvalue and compute the associated eigenfunctions. The extension to spatial stability analysis is also considered. The discretizations studied include: a second-order finite-difference method, a fourth-order accurate two-point compact difference scheme, and a Chebyshev spectral collocation method. Eigenvalue results are presented for Mach numbers up to 10. As the Mach number increases, the performance of the spectral method deteriorates due to the outward movement of the critical layer. To alleviate this problem, a multi-domain spectral collocation method is developed which exhibits better convergence. The overall performance of the fourth-order compact scheme is excellent. Our results also indicate that, in the limit of vanishing Mach number, there exist stable discrete modes in addition to the discrete modes of the Orr–Sommerfeld equation. © 1990 Academic Press, Inc.

1. INTRODUCTION

This paper deals with the numerical solution of the eigenvalue problem associated with the linear stability of compressible boundary layers. The compressible analogue of the well-known Orr–Sommerfeld equation is a coupled set of five ordinary differential equations. These include three second-order momentum equations, one second-order energy equation, and one first-order continuity equation. Following the approach used by Lees and Lin [1], this system may be reduced to a set of eight first-order ordinary differential equations [2–3]. For high Mach number flows, real gas effects become important. If the real gas is considered to be a reacting mixture of perfect gases in chemical equilibrium, then the order of the governing stability equations remains the same. If the mixture is in non-equilibrium due to finite-rate reactions, the species continuity equations must be solved coupled with the fluid mechanics equations. The order of the governing equations then increases according to the number of species included in the gas model. In this paper, we describe the numerical methods as they are applicable to the perfect gas equations. The extension to real gas systems does not offer any complications, at least, conceptually.

The numerical schemes used for solving the compressible linear stability problem may be broadly classified into initial value methods (IVM) and boundary value methods (BVM). Mack [2–3] perfected the use of initial value methods for compressible boundary layer stability. This method consists of constructing independent initial value problems whose solutions satisfy the eighth-order set of differential equations and conditions at the free-stream boundary. The solution is integrated towards the solid boundary by using Runge–Kutta integration and it is required that a linear combination of the solutions satisfies the boundary conditions at the wall. In other words, the relevant characteristic determinant is made to vanish, thus yielding the eigenvalue of the differential system. The problem associated with the growth of the parasitic errors is treated by using the Gram–Schmidt orthonormalization procedure at selected integration steps. In Mack's code, this procedure is automated. Another computer code has been devised by Scott and Watts [4] where this procedure is used for the solution of two-point boundary value problems. This code has also been used for compressible linear stability by several researchers. The main advantage of IVMs is the minimal computer memory requirement and their capacity to adjust the integration to local conditions. The disadvantage is that they require a good guess of the eigenvalue. For spatial stability of high Mach number flows this may require that the eigenvalue be known to be accurate to three or four decimal places for the method to converge. This also means that there is always a risk of missing some modes.

In a boundary value method (BVM) the differential equations are reduced to linear algebraic equations using either a finite-difference discretization or a spectral representation. The global eigenvalues can be obtained by solving the characteristic determinant of a generalized eigenvalue problem. The number of eigenvalues thus obtained is proportional to the number of grid points used. If a guess of the eigenvalue is available, then the eigenvalue may be purified by a local eigenvalue search procedure involving matrix inversion and Newton iteration. The methods of Orszag [5] for the Orr–Sommerfeld problem and Malik and Orszag [6] for the compressible stability problem are examples of boundary value methods. The main advantage of BVMs is their ability to yield eigenvalues when no knowledge of the instability is available for the problem of interest. Suitable transformations may be constructed to resolve optimally the critical layers. The disadvantage of BVMs lies in their higher demand on computational resources, both memory and time. However, for local eigenvalue search, some BVM methods may outperform IVMs in computer time requirements. The method of Malik, Chuang, and Hussaini [7] is an example of such a BVM method.

In an incompressible boundary layer flow, the critical layer lies close to the wall. Methods based upon the Chebyshev spectral approach are a natural choice for BVM schemes since Chebyshev polynomials resolve the boundary regions extremely well. This is the reason for the success of the method of Orszag [5] and Bridges and Morris [8]. Both these methods are based upon Chebyshev spectral-tau approach. Herbert [9] and Spalart [10] have applied spectral collocation techniques to the Orr–Sommerfeld problem. Bramley [11] used the method for the

pipe Poiseuille flow. Recently, Khorrami, Malik, and Ash [12] have developed a Chebyshev spectral collocation method for the stability of incompressible, confined, and unconfined vortical flows. In [12], the governing equations were represented in the primitive variable formulation so that the method is easily extended to the compressible linear stability analysis.

As the Mach number increases, the critical layer moves away from the wall towards the edge of the boundary layer. For example, the critical layer lies in the neighborhood of 0.2δ for $M=0$ and at 0.9δ for $M=10$, where δ is the boundary layer thickness. This suggests that Chebyshev spectral methods may not be a natural choice for hypersonic boundary layer stability. In this paper we compare four methods of solution and study their performance as the Mach number is increased. The first method is based upon a second-order finite-difference discretization used by Malik and Orszag [6]. The second method is another finite-difference scheme which is fourth-order accurate and was developed by Malik, Chuang, and Hussaini [7]. The third method is based upon Chebyshev spectral collocation and is an extension of the method of Khorrami, Malik, and Ash [12] to compressible flows. Finally, we develop a new multi-domain spectral collocation scheme for application to the stability of high speed flows. All these methods belong to the class of methods labelled BVM above.

2. THE GOVERNING EQUATIONS

The Navier–Stokes equations governing the flow of a viscous compressible ideal gas are

$$\rho \left[\frac{\partial q}{\partial t} + (q \cdot \nabla) q \right] = -\nabla p + \nabla \cdot [\lambda (\nabla \cdot q) \bar{I}] + \nabla \cdot [\mu (\nabla q + \nabla q^T)] \quad (2.1)$$

$$\frac{\partial \rho}{\partial t} + \nabla \cdot (\rho q) = 0 \quad (2.2)$$

$$\rho c_p \left[\frac{\partial \tau}{\partial t} + (q \cdot \nabla) \tau \right] = \nabla \cdot (k \nabla \tau) + \frac{\partial p}{\partial t} + (q \cdot \nabla) p + \Phi \quad (2.3)$$

$$p = \rho \Re \tau, \quad (2.4)$$

where q is the velocity vector, ρ the density, p the pressure, τ the temperature, \Re the gas constant, c_p the specific heat, k the thermal conductivity, μ the first coefficient of viscosity, and λ the second coefficient of viscosity. The viscous dissipation Φ is given as

$$\Phi = \lambda (\nabla \cdot q)^2 + \frac{\mu}{2} [\nabla q + \nabla q^T]^2. \quad (2.5)$$

The governing equations for the steady, basic flow may be derived by invoking the boundary layer assumption. The stability equations are then derived by

assuming small disturbances superposed on the basic flow and substituting in the above Navier-Stokes equations. Though real gas effects become important at hypersonic speeds in atmospheric flight, we consider ideal gas flow since the numerical methods developed here would be applicable to the real gas conditions.

Basic Flow

We consider boundary-layer flow past two-dimensional or axisymmetric bodies. The governing equations for the basic state whose stability is the subject of this paper can be derived using the Mangler-Levy-Lees transformation

$$d\zeta = \rho_e \mu_e u_e (r_0(x)/L_r)^{2j} dx \quad (2.6)$$

$$d\eta = [\rho_e u_e / (2\zeta)^{1/2}] (r/L_r)' (\rho/\rho_e) dy, \quad (2.7)$$

where ρ_e is the edge density, μ_e the edge viscosity, u_e the streamwise edge velocity, r_0 the body radius, L_r a reference length, x the distance along the body, and y normal to it. The exponent $j=0$ for a two-dimensional body and $j=1$ for an axisymmetric body. In $\zeta - \eta$ coordinates, the governing equations for the boundary layer flow may be written as [13]

$$(cf'')' + ff' + \bar{\beta}[\rho_e/\rho - (f')^2] = 2\zeta \left(f' \frac{\partial f'}{\partial \zeta} - f'' \frac{\partial f}{\partial \zeta} \right) \quad (2.8)$$

$$(a_1 g' + a_2 f' f'')' + fg' = 2\zeta \left(f' \frac{\partial g}{\partial \zeta} - g' \frac{\partial f}{\partial \zeta} \right), \quad (2.9)$$

where

$$f' \equiv u/u_e, \quad c \equiv (1 + \chi)^{2j} \rho \mu / \rho_e \mu_e,$$

$$\bar{\beta} \equiv (2\zeta/u_e)(du_e/d\zeta),$$

$$g \equiv H/H_e, \quad a_1 \equiv c/\sigma, \quad a_2 \equiv \frac{(\gamma - 1)M^2}{1 + \left(\frac{\gamma - 1}{2}\right)M^2} \left(1 - \frac{1}{\sigma}\right) c$$

and χ is the transverse curvature parameter, $\bar{\beta}$ the pressure gradient parameter, H the enthalpy, γ the ratio of specific heats, and M the edge Mach number defined as

$$M = \frac{u_e}{\sqrt{\gamma \Re T_e}}. \quad (2.10)$$

The Prandtl number σ is defined as

$$\sigma = \frac{\mu c_p}{k}, \quad (2.11)$$

where c_p is the specific heat at constant pressure and is assumed to be constant. The viscosity μ is assumed to be given by the Sutherland formula,

$$\mu = 2.27 \times 10^{-8} \frac{T^{1/2}}{1 + 198.6/T} \text{ lb-sec/ft}^2.$$

The thermal conductivity k may also be prescribed by a similar formula. For the results presented in this paper, however, we compute it by assuming $\sigma = 0.7$.

For a flat plate with no pressure gradient, the above equations (2.8)–(2.9) reduce to

$$(cf''')' + ff'' = 0 \quad (2.12)$$

$$(a_1 g' + a_2 f'f'')' + fg' = 0 \quad (2.13)$$

which have been solved by a fourth-order accurate compact difference scheme [7] and Newton's iteration method. No slip boundary conditions were used for either an insulated wall or for a specified wall temperature.

Compressible Linear Stability Equations

We use Cartesian coordinates x, y, z , where x is the streamwise direction, z the spanwise direction and y is normal to the solid boundary. All the lengths are assumed scaled by a reference length ℓ , velocities by u_e , density by ρ_e , pressure by $\rho_e u_e^2$, time by ℓ/u_e and other variables by their corresponding boundary layer edge values. The instantaneous values of velocities, u, v, w , pressure p , temperature τ , density ρ , may be represented as the sum of a mean and a fluctuation quantity, i.e.,

$$\begin{aligned} u &= \bar{U} + \tilde{u}, & v &= \bar{V} + \tilde{v}, & w &= \bar{W} + \tilde{w} \\ p &= \bar{P} + \tilde{p}, & \tau &= \bar{T} + \tilde{\tau}, & \rho &= \bar{\rho} + \tilde{\rho} \\ \mu &= \bar{\mu} + \tilde{\mu}, & \lambda &= \bar{\lambda} + \tilde{\lambda}, & k &= \bar{k} + \tilde{k}. \end{aligned}$$

Substituting these into the nondimensional form of the governing equations (2.1)–(2.4) yields the **linearized perturbation equations** (after dropping “bars” from the mean quantities)

$$\begin{aligned} & \rho \left(\frac{\partial \tilde{u}}{\partial t} + U \frac{\partial \tilde{u}}{\partial x} + \tilde{u} \frac{\partial U}{\partial x} + V \frac{\partial \tilde{u}}{\partial y} + \tilde{v} \frac{\partial U}{\partial y} + W \frac{\partial \tilde{u}}{\partial z} + \tilde{w} \frac{\partial U}{\partial z} \right) \\ & + \tilde{\rho} \left(U \frac{\partial U}{\partial x} + V \frac{\partial U}{\partial y} + W \frac{\partial U}{\partial z} \right) \\ & = -\frac{\partial \tilde{p}}{\partial x} + \frac{1}{R} \left\{ \frac{\partial}{\partial x} \left[\mu \left(l_2 \frac{\partial \tilde{u}}{\partial x} + l_0 \frac{\partial \tilde{v}}{\partial y} + l_0 \frac{\partial \tilde{w}}{\partial z} \right) + \tilde{\mu} \left(l_2 \frac{\partial U}{\partial x} + l_0 \frac{\partial V}{\partial y} + l_0 \frac{\partial W}{\partial z} \right) \right] \right. \\ & + \frac{\partial}{\partial y} \left[\mu \left(\frac{\partial \tilde{u}}{\partial y} + \frac{\partial \tilde{v}}{\partial x} \right) + \tilde{\mu} \left(\frac{\partial U}{\partial y} + \frac{\partial V}{\partial x} \right) \right] \\ & \left. + \frac{\partial}{\partial z} \left[\mu \left(\frac{\partial \tilde{w}}{\partial x} + \frac{\partial \tilde{u}}{\partial z} \right) + \tilde{\mu} \left(\frac{\partial W}{\partial x} + \frac{\partial U}{\partial z} \right) \right] \right\}, \end{aligned} \quad (2.14)$$

$$\begin{aligned}
& \rho \left(\frac{\partial \tilde{v}}{\partial t} + U \frac{\partial \tilde{v}}{\partial x} + \tilde{u} \frac{\partial V}{\partial x} + V \frac{\partial \tilde{v}}{\partial y} + \tilde{v} \frac{\partial V}{\partial y} + W \frac{\partial \tilde{v}}{\partial z} + \tilde{w} \frac{\partial V}{\partial z} \right) \\
& + \tilde{\rho} \left(U \frac{\partial V}{\partial x} + V \frac{\partial V}{\partial y} + W \frac{\partial V}{\partial z} \right) \\
& = -\frac{\partial \tilde{p}}{\partial y} + \frac{1}{R} \left\{ \frac{\partial}{\partial x} \left[\mu \left(\frac{\partial \tilde{u}}{\partial y} + \frac{\partial \tilde{v}}{\partial x} \right) + \tilde{\mu} \left(\frac{\partial U}{\partial y} + \frac{\partial V}{\partial x} \right) \right] \right. \\
& + \frac{\partial}{\partial y} \left[\mu \left(l_0 \frac{\partial \tilde{u}}{\partial x} + l_2 \frac{\partial \tilde{v}}{\partial y} + l_0 \frac{\partial \tilde{w}}{\partial z} \right) + \tilde{\mu} \left(l_2 \frac{\partial V}{\partial y} + l_0 \frac{\partial U}{\partial x} + l_0 \frac{\partial W}{\partial z} \right) \right. \\
& \left. \left. + \frac{\partial}{\partial z} \left[\mu \left(\frac{\partial \tilde{v}}{\partial z} + \frac{\partial \tilde{w}}{\partial y} \right) + \tilde{\mu} \left(\frac{\partial V}{\partial z} + \frac{\partial W}{\partial y} \right) \right] \right] \right\}, \quad (2.15)
\end{aligned}$$

$$\begin{aligned}
& \rho \left(\frac{\partial \tilde{w}}{\partial t} + U \frac{\partial \tilde{w}}{\partial x} + \tilde{u} \frac{\partial W}{\partial x} + V \frac{\partial \tilde{w}}{\partial y} + \tilde{v} \frac{\partial W}{\partial y} + W \frac{\partial \tilde{w}}{\partial z} + \tilde{w} \frac{\partial W}{\partial z} \right) \\
& + \tilde{\rho} \left(U \frac{\partial W}{\partial x} + V \frac{\partial W}{\partial y} + W \frac{\partial W}{\partial z} \right) \\
& = -\frac{\partial \tilde{p}}{\partial z} + \frac{1}{R} \left\{ \frac{\partial}{\partial x} \left[\mu \left(\frac{\partial \tilde{w}}{\partial x} + \frac{\partial \tilde{u}}{\partial z} \right) + \tilde{\mu} \left(\frac{\partial W}{\partial x} + \frac{\partial U}{\partial z} \right) \right] \right. \\
& + \frac{\partial}{\partial y} \left[\mu \left(\frac{\partial \tilde{v}}{\partial z} + \frac{\partial \tilde{w}}{\partial y} \right) + \tilde{\mu} \left(\frac{\partial V}{\partial z} + \frac{\partial W}{\partial y} \right) \right] \\
& \left. + \frac{\partial}{\partial z} \left[\mu \left(l_0 \frac{\partial \tilde{u}}{\partial x} + l_0 \frac{\partial \tilde{v}}{\partial y} + l_2 \frac{\partial \tilde{w}}{\partial z} \right) + \tilde{\mu} \left(l_0 \frac{\partial U}{\partial x} + l_0 \frac{\partial V}{\partial y} + l_2 \frac{\partial W}{\partial z} \right) \right] \right\}, \quad (2.16)
\end{aligned}$$

$$\frac{\partial \tilde{p}}{\partial t} + \frac{\partial}{\partial x} (\rho \tilde{u} + \tilde{\rho} U) + \frac{\partial}{\partial y} (\rho \tilde{v} + \tilde{\rho} V) + \frac{\partial}{\partial z} (\rho \tilde{w} + \tilde{\rho} W) = 0, \quad (2.17)$$

$$\begin{aligned}
& \rho \left[\frac{\partial \tilde{T}}{\partial t} + \tilde{u} \frac{\partial T}{\partial x} + U \frac{\partial \tilde{T}}{\partial x} + \tilde{v} \frac{\partial T}{\partial y} + V \frac{\partial \tilde{T}}{\partial y} + \tilde{w} \frac{\partial T}{\partial z} + W \frac{\partial \tilde{T}}{\partial z} \right] \\
& + \tilde{\rho} \left[U \frac{\partial T}{\partial x} + V \frac{\partial T}{\partial y} + W \frac{\partial T}{\partial z} \right] \\
& = (\gamma - 1) M^2 \left[\frac{\partial \tilde{p}}{\partial t} + \tilde{u} \frac{\partial P}{\partial x} + U \frac{\partial \tilde{p}}{\partial x} + V \frac{\partial \tilde{p}}{\partial y} + \tilde{v} \frac{\partial P}{\partial y} + \tilde{w} \frac{\partial P}{\partial z} + W \frac{\partial \tilde{p}}{\partial z} \right] \\
& + \frac{1}{R \text{Pr}} \left[\frac{\partial}{\partial x} \left(k \frac{\partial \tilde{T}}{\partial x} + \tilde{k} \frac{\partial T}{\partial x} \right) + \frac{\partial}{\partial y} \left(k \frac{\partial \tilde{T}}{\partial y} + \tilde{k} \frac{\partial T}{\partial y} \right) + \frac{\partial}{\partial z} \left(k \frac{\partial \tilde{T}}{\partial z} + \tilde{k} \frac{\partial T}{\partial z} \right) \right] \\
& + (\gamma - 1) M^2 \frac{\mu}{R} \left\{ 2l_2 \left(\frac{\partial U}{\partial x} \frac{\partial \tilde{u}}{\partial x} + \frac{\partial V}{\partial y} \frac{\partial \tilde{v}}{\partial y} + \frac{\partial W}{\partial z} \frac{\partial \tilde{w}}{\partial z} \right) \right.
\end{aligned}$$

$$\begin{aligned}
& + 2l_0 \left[\frac{\partial U}{\partial x} \left(\frac{\partial \tilde{v}}{\partial y} + \frac{\partial \tilde{w}}{\partial z} \right) + \frac{\partial V}{\partial y} \left(\frac{\partial \tilde{u}}{\partial x} + \frac{\partial \tilde{w}}{\partial z} \right) + \frac{\partial W}{\partial z} \left(\frac{\partial \tilde{u}}{\partial x} + \frac{\partial \tilde{v}}{\partial y} \right) \right] \\
& + 2 \left(\frac{\partial \tilde{u}}{\partial y} + \frac{\partial \tilde{v}}{\partial x} \right) \left(\frac{\partial U}{\partial y} + \frac{\partial V}{\partial x} \right) + 2 \left(\frac{\partial \tilde{v}}{\partial z} + \frac{\partial \tilde{w}}{\partial y} \right) \left(\frac{\partial V}{\partial z} + \frac{\partial W}{\partial y} \right) \\
& + 2 \left(\frac{\partial \tilde{u}}{\partial z} + \frac{\partial \tilde{w}}{\partial x} \right) \left(\frac{\partial U}{\partial z} + \frac{\partial W}{\partial x} \right) \Big\} \\
& + (\gamma - 1) M^2 \frac{\tilde{\mu}}{R} \left\{ l_2 \left[\left(\frac{\partial U}{\partial x} \right)^2 + \left(\frac{\partial V}{\partial y} \right)^2 + \left(\frac{\partial W}{\partial z} \right)^2 \right] \right. \\
& + 2l_0 \left(\frac{\partial U}{\partial x} \frac{\partial V}{\partial y} + \frac{\partial U}{\partial x} \frac{\partial W}{\partial z} + \frac{\partial V}{\partial y} \frac{\partial W}{\partial z} \right) + \left(\frac{\partial U}{\partial y} + \frac{\partial V}{\partial x} \right)^2 \\
& \left. + \left(\frac{\partial V}{\partial z} + \frac{\partial W}{\partial y} \right)^2 + \left(\frac{\partial U}{\partial z} + \frac{\partial W}{\partial x} \right)^2 \right\}, \tag{2.18}
\end{aligned}$$

$$\tilde{\rho} = \gamma M^2 \frac{\tilde{P}}{T} - \frac{\rho}{T} \tilde{T}, \tag{2.19}$$

where $R = \rho_e u_e \ell / \mu_e$ is the Reynolds number, $Pr = c_p \mu_e / k_e$ is the Prandtl number, γ is the ratio of the specific heats, and $l_j = j + \lambda / \mu$. The mean equation of state is

$$\gamma M^2 P = \rho T. \tag{2.20}$$

We consider the stability of locally parallel compressible boundary layer flow. The "locally parallel flow" assumption is the same as used in the application of the Orr-Sommerfeld equation to the incompressible boundary layer flow. Under this assumption,

$$\begin{aligned}
U &= U(y), & V &= 0, & W &= W(y) \\
T &= T(y), & \rho &= \rho(y).
\end{aligned} \tag{2.21}$$

Due to the boundary layer assumption, P (see Eq. (2.20)) is constant across the layer and is equal to $1/\gamma M^2$. In that case $\rho = 1/T$ and Eq. (2.19) simplifies to

$$\tilde{\rho} = \gamma M^2 \frac{\tilde{P}}{T} - \frac{\tilde{T}}{T^2}. \tag{2.22}$$

Equation (2.22) can be used to eliminate density $\tilde{\rho}$ from Eq. (2.14)–(2.18). Furthermore, we can write

$$\tilde{\mu} = \frac{d\mu}{dT} \tilde{T}, \quad \tilde{\lambda} = \frac{d\lambda}{dT} \tilde{T}, \quad \tilde{k} = \frac{dk}{dT} \tilde{T}. \tag{2.23}$$

Using Eq. (2.21)–(2.23), the governing equations (2.14)–(2.18) simplify to

$$\begin{aligned}
 & \left(\frac{\partial \tilde{u}}{\partial t} + U \frac{\partial \tilde{u}}{\partial x} + \tilde{v} \frac{dU}{dy} + W \frac{\partial \tilde{u}}{\partial z} \right) / T \\
 &= -\frac{\partial \tilde{p}}{\partial x} + \frac{\mu}{R} \left[l_2 \frac{\partial^2 \tilde{u}}{\partial x^2} + l_1 \left(\frac{\partial^2 \tilde{v}}{\partial x \partial y} + \frac{\partial^2 \tilde{w}}{\partial x \partial z} \right) \right. \\
 &\quad \left. + \frac{\partial^2 \tilde{u}}{\partial y^2} + \frac{\partial^2 \tilde{u}}{\partial z^2} + \frac{1}{\mu} \frac{d\mu}{dT} \frac{dT}{dy} \left(\frac{\partial \tilde{u}}{\partial y} + \frac{\partial \tilde{v}}{\partial x} \right) \right. \\
 &\quad \left. + \frac{1}{\mu} \frac{d\mu}{dT} \left(\frac{d^2 U}{dy^2} \tilde{T} + \frac{dU}{dy} \frac{\partial \tilde{T}}{\partial y} \right) + \frac{1}{\mu} \frac{d^2 \mu}{dT^2} \frac{dT}{dy} \frac{dU}{dy} \tilde{T} \right], \quad (2.24)
 \end{aligned}$$

$$\begin{aligned}
 & \left(\frac{\partial \tilde{v}}{\partial t} + U \frac{\partial \tilde{v}}{\partial x} + W \frac{\partial \tilde{v}}{\partial z} \right) / T \\
 &= -\frac{\partial \tilde{p}}{\partial y} + \frac{\mu}{R} \left[\frac{\partial^2 \tilde{v}}{\partial x^2} + l_1 \left(\frac{\partial^2 \tilde{u}}{\partial x \partial y} + \frac{\partial^2 \tilde{w}}{\partial y \partial z} \right) \right. \\
 &\quad \left. + l_2 \frac{\partial^2 \tilde{v}}{\partial y^2} + \frac{\partial^2 \tilde{v}}{\partial z^2} + \frac{1}{\mu} \frac{d\mu}{dT} \left(\frac{\partial \tilde{T}}{\partial x} \frac{dU}{dy} + \frac{\partial \tilde{T}}{\partial z} \frac{dW}{dy} \right) \right. \\
 &\quad \left. + \frac{1}{\mu} \frac{d\mu}{dT} \frac{dT}{dy} \left\{ l_0 \left(\frac{\partial \tilde{u}}{\partial x} + \frac{\partial \tilde{w}}{\partial z} \right) + l_2 \frac{\partial \tilde{v}}{\partial y} \right\} \right], \quad (2.25)
 \end{aligned}$$

$$\begin{aligned}
 & \left(\frac{\partial \tilde{w}}{\partial t} + U \frac{\partial \tilde{w}}{\partial x} + \tilde{v} \frac{dW}{dy} + W \frac{\partial \tilde{w}}{\partial z} \right) / T \\
 &= -\frac{\partial \tilde{p}}{\partial z} + \frac{\mu}{R} \left[\frac{\partial^2 \tilde{w}}{\partial x^2} + l_1 \left(\frac{\partial^2 \tilde{u}}{\partial x \partial z} + \frac{\partial^2 \tilde{v}}{\partial y \partial z} \right) \right. \\
 &\quad \left. + \frac{\partial^2 \tilde{w}}{\partial y^2} + l_2 \frac{\partial^2 \tilde{w}}{\partial z^2} + \frac{1}{\mu} \frac{d\mu}{dT} \frac{dT}{dy} \left(\frac{\partial \tilde{v}}{\partial z} + \frac{\partial \tilde{w}}{\partial y} \right) \right. \\
 &\quad \left. + \frac{1}{\mu} \frac{d\mu}{dT} \left(\frac{d^2 W}{dy^2} \tilde{T} + \frac{dW}{dy} \frac{\partial \tilde{T}}{\partial y} \right) + \frac{1}{\mu} \frac{d^2 \mu}{dT^2} \frac{dT}{dy} \frac{dW}{dy} \tilde{T} \right], \quad (2.26)
 \end{aligned}$$

$$\begin{aligned}
 & \frac{\gamma M^2}{T} \frac{\partial \tilde{p}}{\partial t} - \frac{1}{T^2} \frac{\partial \tilde{T}}{\partial t} + \frac{1}{T} \frac{\partial \tilde{u}}{\partial x} + U \left(\frac{\gamma M^2}{T} \frac{\partial \tilde{p}}{\partial x} - \frac{1}{T^2} \frac{\partial \tilde{T}}{\partial x} \right) \\
 &+ \frac{1}{T} \frac{\partial \tilde{v}}{\partial y} - \frac{1}{T^2} \frac{dT}{dy} \tilde{v} + \frac{1}{T} \frac{\partial \tilde{w}}{\partial z} + W \left(\frac{\gamma M^2}{T} \frac{\partial \tilde{p}}{\partial z} - \frac{1}{T^2} \frac{\partial \tilde{T}}{\partial z} \right) = 0, \quad (2.27)
 \end{aligned}$$

$$\begin{aligned}
& \left(\frac{\partial \tilde{T}}{\partial t} + U \frac{\partial \tilde{T}}{\partial x} + \tilde{v} \frac{dT}{dy} + W \frac{\partial \tilde{T}}{\partial z} \right) / T \\
&= (\gamma - 1) M^2 \left[\frac{\partial \tilde{p}}{\partial t} + U \frac{\partial \tilde{p}}{\partial x} + W \frac{\partial \tilde{p}}{\partial z} \right] \\
&+ \frac{\mu}{R\sigma} \left[\frac{\partial^2 \tilde{T}}{\partial x^2} + \frac{\partial^2 \tilde{T}}{\partial y^2} + \frac{\partial^2 \tilde{T}}{\partial z^2} + \frac{2}{k} \frac{dk}{dT} \frac{dT}{dy} \frac{\partial \tilde{T}}{\partial y} \right. \\
&+ \left. \left(\frac{1}{k} \frac{dk}{dT} \frac{d^2 T}{dy^2} + \frac{1}{k} \frac{d^2 k}{dT^2} \left(\frac{dT}{dy} \right)^2 \right) \tilde{T} \right] \\
&+ (\gamma - 1) M^2 \frac{\mu}{R} \left[2 \frac{dU}{dy} \left(\frac{\partial \tilde{u}}{\partial y} + \frac{\partial \tilde{v}}{\partial x} \right) \right. \\
&+ \left. 2 \frac{dW}{dy} \left(\frac{\partial \tilde{v}}{\partial z} + \frac{\partial \tilde{w}}{\partial y} \right) + \frac{1}{\mu} \frac{d\mu}{dT} \left(\left(\frac{dU}{dy} \right)^2 + \left(\frac{dW}{dy} \right)^2 \right) \right], \quad (2.28)
\end{aligned}$$

where σ is the variable Prandtl number defined in Eq. (2.11).

We may now assume that the **velocity, pressure, and temperature fluctuations** may be represented by a **harmonic wave of the form**

$$(\tilde{u}, \tilde{v}, \tilde{w}) = [\hat{u}(y), \hat{v}(y), \hat{w}(y)] e^{i(\alpha x + \beta z - \omega t)} \quad (2.29)$$

$$\tilde{p} = \hat{p}(y) e^{i(\alpha x + \beta z - \omega t)} \quad (2.30)$$

$$\tilde{T} = \hat{T}(y) e^{i(\alpha x + \beta z - \omega t)}, \quad (2.31)$$

where α, β are the wavenumbers and ω is the frequency which, in general, are all complex. In temporal stability theory, α, β are assumed to be real and ω is complex while the converse is true in the spatial stability theory.

Substituting Eqs. (2.29)–(2.31) into Eqs. (2.24)–(2.28), it can be shown that the linear disturbances satisfy the following system of ordinary differential equations

$$(AD^2 + BD + C)\phi = 0, \quad (2.32)$$

where ϕ is a five-element vector defined by

$$\{\hat{u}, \hat{v}, \hat{p}, \hat{T}, \hat{w}\}^{\text{tr}}.$$

Here $D \equiv d/dy$, while A is given as

$$A = \begin{bmatrix} 1 & & & & 0 \\ & 1 & & & \\ & & 0 & & \\ 0 & & & 1 & \\ & & & & 1 \end{bmatrix}$$

and B, C are 5×5 matrices whose nonzero elements are given in Appendix I. Since

we are interested in two-dimensional basic flow here, the velocity component $W(y)$ may be set to zero in the Appendix. For two-dimensional disturbances, the order of the system is reduced as \hat{w} momentum equation may be dropped.

The boundary conditions for Eq. (2.32) are

$$y = 0; \quad \phi_1 = \phi_2 = \phi_4 = \phi_5 = 0 \quad (2.33)$$

$$y \rightarrow \infty; \quad \phi_1, \phi_2, \phi_4, \phi_5 \rightarrow 0. \quad (2.34)$$

Here temperature perturbations are assumed to vanish at the solid boundary whereas the mean flow may be treated with an insulated wall. This is a reasonable assumption for high frequency disturbances where the temperature fluctuations will not penetrate deep into the solid boundary due to the thermal inertia of the solid body. In other words, the wall will appear insulated on the time scale of the mean flow but not on the short time scales of the disturbances. However, for stationary disturbances (such as crossflow and Görtler), one may need to replace $\phi_4(0) = 0$ in favor of $d\phi_4(0)/dy$ or a combination thereof, depending upon the physical properties of the solid and the gas. The numerical methods that we describe could easily accommodate Neumann or mixed boundary conditions on temperature fluctuations.

Equations (2.32)–(2.34) constitute an eigenvalue problem described by the complex dispersion relation

$$\omega = \omega(\alpha, \beta) \quad (2.35)$$

and the determination of this relation is essentially the subject of this paper.

Using the continuity equation, the second-order normal momentum equation may be reduced to a first-order equation for pressure. Thus the above linear stability equations (2.32) may also be rewritten as a system of eight first-order equations

$$\frac{d\psi_i}{dy} = \sum_{j=1}^8 a_{ij}\psi_j; \quad i = 1, 2, \dots, 8, \quad (2.36)$$

where

$$\begin{aligned} \psi_1 &= \phi_1, & \psi_2 &= \frac{d\psi_1}{dy}, & \psi_3 &= \phi_2, & \psi_4 &= \phi_3, \\ \psi_5 &= \phi_4, & \psi_6 &= \frac{d\psi_5}{dy}, & \psi_7 &= \phi_5, & \psi_8 &= \frac{d\psi_7}{dy} \end{aligned}$$

with corresponding boundary conditions

$$y = 0; \quad \psi_1 = \psi_3 = \psi_5 = \psi_7 = 0 \quad (2.37)$$

$$y \rightarrow \infty; \quad \psi_1, \psi_3, \psi_5, \psi_7 \rightarrow 0. \quad (2.38)$$

The coefficients a_{ij} are given in Appendix II.

We note here that the governing set of five stability equations represented by Eq. (2.32) was derived by eliminating perturbation density from the continuity equation using the equation of state. This is only done to reduce the required computational work. One may also solve the system containing the (algebraic) equation of state coupled with the five differential equations (without eliminating density perturbations). This was indeed done by using the 2FD scheme described below and the computed eigenvalue spectrum was similar to that given by Eq. (2.32).

3. NUMERICAL METHODS FOR STABILITY EQUATIONS

There are two classes of numerical methods that can be used for computing the eigenvalues: **global and local methods**. For the global method a generalized eigenvalue problem is set up and the eigenvalues are obtained by using standard algorithms such as LR or QR or QZ. **These algorithms yield all the eigenvalues of the discretized system and a guess for the eigenvalues is not required.** In a local method, a guess for the eigenvalue is required. Only the eigenvalue which happens to lie in the neighborhood of the guessed value is computed using iterative techniques such as Newton's method. Global and local methods may use the same discretization. Global methods are computationally much more expensive than the local methods since they compute all the eigenvalues of the discretized system. Thus, the only rationale for using the global method is **if no guess for the eigenvalue is available** or **if the whole spectrum of eigenvalues is desired**. In the spatial stability of hypersonic boundary layers, several modes could lie close by and local methods fail to converge under these circumstances unless an extremely good guess for the desired instability mode is available. So, the global methods are particularly valuable for the hypersonic boundary layer stability problem.

The methods we describe below could fall in the categories of both the global or local methods. However, we characterize them by the discretization used. The methods are first described for temporal stability where wave numbers α , β are known and the desired eigenvalue is the complex frequency ω . The extension to spatial stability where ω is known and α is sought will be discussed in a later section.

Second-Order Finite-Difference (2FD) Method

The governing system of Eqs. (2.32) is represented using a **second-order accurate finite-difference formula** on a **staggered mesh** (see Fig. 1).

First the boundary layer coordinate y , $0 \leq y \leq y_{\max}$, is mapped onto the computational domain $0 \leq \eta \leq 1$ by the algebraic mapping

$$y = \frac{a\eta}{b - \eta}, \quad (3.1)$$

where $b = 1 + a/y_{\max}$. Here y_{\max} is the location where free-stream boundary conditions are satisfied and a is a scaling parameter chosen to optimize the accuracy of

(FREE STREAM)

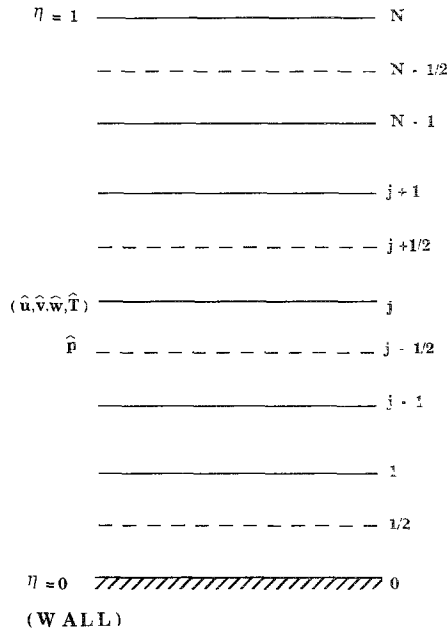


FIG. 1. A schematic of the staggered grid used for 2FD scheme.

the calculations. Here we use $a = y_{\max} y_i / (y_{\max} - 2y_i)$ which puts half the node points used for discretization between $y = 0$ and $y = y_i$.

The computational domain η is divided into equal intervals and the second-order equations are represented as

$$\begin{aligned}
 f_1 A_j \left[\frac{\phi_{j+1} - 2\phi_j + \phi_{j-1}}{\Delta\eta^2} \right] + d_1 \left[(f_2 A_j + f_3 B_j) \left(\frac{\phi_{j+1} - \phi_{j-1}}{2\Delta\eta} \right) + C_j \phi_j \right] \\
 + d_2 \left[f_3 B_j \left(\frac{\phi_{j+1/2} - \phi_{j-1/2}}{\Delta\eta} \right) + C_j \left(\frac{\phi_{j+1/2} + \phi_{j-1/2}}{2} \right) \right] = 0 \quad (j = 1, \dots, N-1),
 \end{aligned} \tag{3.2}$$

where ϕ_j is the value of ϕ at $\eta = j/N$ and has components ϕ_{kj} ($k = 1, \dots, 5$). Also, $d_1 = 1$, $d_2 = 0$, except $d_1 = 0$, $d_2 = 1$ for the \hat{p} component of ϕ , and

$$\begin{aligned}
 f_1 &= \frac{(b-\eta)^4}{b^2 a^2} \\
 f_2 &= -\frac{2(b-\eta)^3}{b^2 a^2} \\
 f_3 &= \frac{(b-\eta)^2}{ba}.
 \end{aligned}$$

The first-order continuity equation is represented as

$$f_3 B_{j+1/2} \frac{\phi_{j+1} - \phi_j}{\Delta \eta} + C_{j+1/2} \phi_{j+1/2} = 0 \quad (j=0, \dots, N-1). \quad (3.3)$$

Equations (3.2)–(3.3) along with the eight boundary conditions (2.33)–(2.34) represent $5N+4$ equations for $5N+4$ unknowns. Since the velocity and temperature disturbances are assumed to be identically zero at the solid boundary ($\eta=0$) the system reduces to $5N$ equations for $5N$ unknowns when these boundary conditions are applied. This is a block-tridiagonal system of equations with 5×5 blocks. Note that no artificial pressure boundary conditions are needed since we use staggered mesh.

When the discretized compressible stability equations (3.2)–(3.3), along with the boundary conditions (2.33)–(2.34) are formulated as a matrix eigenvalue problem, they take the form

$$\bar{A}\phi = \omega \bar{B}\phi, \quad (3.4)$$

where ω is the eigenvalue and ϕ is the discrete representation of the eigenfunction. The eigenvalue is determined by the determinant condition

$$\text{Det} |\bar{A} - \omega \bar{B}| = 0. \quad (3.5)$$

If \bar{B} is invertible then (3.5) may be solved as

$$\text{Det} |\bar{B}^{-1}\bar{A} - \omega I| = 0 \quad (3.6)$$

which is the standard matrix eigenvalue problem, solvable by LR or QR methods [14]. Here $\bar{B}^{-1}\bar{A}$ is a $5N \times 5N$ square matrix. Note that we only need one square matrix to set up and solve the eigenvalue problem since \bar{B} is a block-tridiagonal matrix assuring efficient inversion. For the global problem, the boundary conditions used at $y = y_{\max}$ are

$$\hat{u} = \hat{v} = \hat{T} = \hat{w} = 0. \quad (3.7)$$

This implies that \bar{B} is singular. Of course, the singularity can be removed from the system by explicitly substituting the values of \hat{u} , \hat{v} , \hat{T} , and \hat{w} from Eq. (3.7) into Eqs. (3.2)–(3.3), thus reducing the order of the system to $5N-4$. However, now the inversion of \bar{B} is not simple. An alternative is to replace the boundary conditions (3.7) with conditions at $y = y_{\max}$ as

$$\begin{aligned} \hat{u} &= \omega \varepsilon \hat{u} \\ \hat{v} &= \omega \varepsilon \hat{v} \\ \hat{T} &= \omega \varepsilon \hat{T} \\ \hat{w} &= \omega \varepsilon \hat{w}. \end{aligned} \quad (3.8)$$

This allows efficient computation of $\bar{B}^{-1}\bar{A}$ using block-tridiagonal solvers. The eigenvalue solution using the LR method, for example, simply yields four additional eigenvalues $\omega = \varepsilon$ associated with Eq. (3.8). Values of $\varepsilon = 1$ and 10^{-12} were tried and no effect on the desired physical eigenvalues was observed. This was tested by replacing (3.8) with the actual boundary conditions (3.7) and solving the generalized eigenvalue problem (3.4) by using the QZ algorithm. Use of (3.8) not only eliminates the need for storage of one square matrix, it also enables one to compute the eigenvalues in substantially less computer time as we will discuss in Section 4 below.

Using finite-difference discretization above, a local method was also developed in [6] using the inverse Rayleigh iteration procedure [14]. Now, the boundary conditions at $y = y_{\max}$ are either those given by Eq. (3.7) or those derived from the asymptotic structure of Eq. (2.32) in the free stream. The latter option allows the boundary conditions to be imposed at a lower value of y_{\max} , i.e., just outside the boundary layer. Within the context of finite-difference methods, the local method described below, using a fourth-order accurate compact difference scheme, is to be preferred. We will describe the inverse Rayleigh iteration method within the context of spectral collocation methods.

Fourth-Order Compact Difference (4CD) Scheme

This scheme is suitable for solving eigenvalue problems represented as a system of first-order equations as in Eqs. (2.36). We use the fourth-order accurate two-point scheme which is derived by means of the Euler-Maclaurin formula

$$\Psi^k - \Psi^{k-1} = \frac{h_k}{2} \left(\frac{d\Psi^k}{dy} + \frac{d\Psi^{k-1}}{dy} \right) - \frac{h_k^2}{12} \left(\frac{d^2\Psi^k}{dy^2} - \frac{d^2\Psi^{k-1}}{dy^2} \right) + O(h_k^5), \quad (3.9)$$

where $\Psi^k = \Psi(y_k)$ and $h_k = y_k - y_{k-1}$.

In order to apply this scheme to Eq. (2.36), we set

$$\Psi = \{\psi_i\}, \quad \frac{d\Psi}{dy} = \left\{ \sum_{j=1}^8 a_{ij} \psi_j \right\}, \quad \frac{d^2\Psi}{dy^2} = \left\{ \sum_{j=1}^8 b_{ij} \psi_j \right\},$$

where

$$b_{ij} = \frac{da_{ij}}{dy} + \sum_{l=1}^8 a_{il} a_{lj}$$

and thus Eq. (3.9) becomes

$$\begin{aligned} \psi_i^k - \frac{h_k}{2} \sum_{j=1}^8 a_{ij}^k \psi_j^k + \frac{h_k^2}{12} \sum_{j=1}^8 b_{ij}^k \psi_j^k \\ - \left[\psi_i^{k-1} + \frac{h_k}{2} \sum_{j=1}^8 a_{ij}^{k-1} \psi_j^{k-1} + \frac{h_k^2}{12} \sum_{j=1}^8 b_{ij}^{k-1} \psi_j^{k-1} \right] = 0. \end{aligned} \quad (3.10)$$

As in [7], the above equation system along with the boundary conditions (2.37)–(2.38) can be rewritten in the block-tridiagonal form

$$A_k \Psi^{k-1} + B_k \Psi^k + C_k \Psi^{k+1} = H, \quad (3.11)$$

where A_k , B_k , C_k are 8×8 matrices and H is a 8×1 null matrix. The above equation (3.11) may also be written as

$$L\Psi = H, \quad (3.12)$$

where

$$L = [A_k, B_k, C_k].$$

Since we have eight equations now instead of five, this discretization scheme is not suitable for a global method where it is desirable to keep the order of the equations at its minimum due to computational considerations. For higher accuracy in a global eigenvalue search, we will turn to spectral collocation methods in the next section. An advantage of the present scheme, however, is that for local solution the order of the system remains the same for temporal and spatial stability. This is not the case for global methods as we will discuss later.

For the local eigenvalue problem, we solve the block-tridiagonal system of Eqs. (3.12), using LU factorizations. Note that Eq. (3.12) is homogeneous. In order to avoid a trivial solution, nonhomogeneous boundary conditions are imposed at the wall. Specifically, the boundary condition $\psi_1(0)=0$ is replaced by $\psi_4(0)=1$. This is equivalent to normalizing the eigensolution by the value of the pressure perturbation at the wall. Since pressure does not vanish at the wall, the normalizing condition $\psi_4(0)=1$ is appropriate. Other normalizations are also possible [7]; however, our experience indicates that normalizing with pressure gives the best results in the sense of rate of convergence and radius of convergence.

Since Eq. (3.12) is now nonhomogeneous, a nontrivial solution may be obtained for the guessed eigenvalue $\omega = \omega_0$. Newton's method is then used to iterate on ω such that the missing boundary condition $\psi_1(0)=0$ is satisfied. Thus, when a solution Ψ is obtained for ω_0 , the correction $\Delta\omega$ is determined from the equation

$$\psi_1(0) + \frac{\partial\psi_1(0)}{\partial\omega} \Delta\omega = 0, \quad (3.13)$$

where $\psi_1(0)$ is known from the solution Ψ just obtained; $\partial\psi_1(0)/\partial\omega$ is obtained by solving

$$L \frac{\partial\Psi}{\partial\omega} = -\frac{\partial L}{\partial\omega} \Psi. \quad (3.14)$$

The process is repeated until $\psi_1(0)$ vanishes within preassigned tolerance. Note that Eqs. (3.12) and (3.14) can be solved with the same LU factorizations.

A higher order iterative method may also be derived by using Taylor's series. In this case, Eq. (3.13) is replaced by

$$\psi_1(0) + \frac{\partial \psi_1(0)}{\partial \omega} \Delta \omega + \frac{1}{2} \frac{\partial^2 \psi_1(0)}{\partial \omega^2} \Delta \omega^2 = 0. \quad (3.15)$$

If $\Delta \omega^2$ is substituted in this equation from Eq. (3.13), then we have

$$\Delta \omega \approx -\psi_1(0) \left/ \left(\frac{\partial \psi_1(0)}{\partial \omega} \right) - \psi_1^2(0) \frac{\partial^2 \psi_1(0)}{\partial \omega^2} \right/ 2 \left(\frac{\partial \psi_1(0)}{\partial \omega} \right)^3. \quad (3.16)$$

The new unknown $\partial^2 \psi_1(0)/\partial \omega^2$ is obtained from the solution of

$$L \frac{\partial^2 \Psi}{\partial \omega^2} = -2 \frac{\partial L}{\partial \omega} \frac{\partial \Psi}{\partial \omega} - \frac{\partial^2 L}{\partial \omega^2} \Psi \quad (3.17)$$

which may also be solved by using the same LU factorization as used for the solution of Eq. (3.12).

This higher order scheme converges faster in terms of the number of iterations but there appears to be no significant advantage on computational cost since the work required per iteration increases. The latter scheme does appear to have somewhat larger radius of convergence. In some very sensitive calculations involving the compressible Görtler instability, the higher order scheme converged while it became difficult to obtain eigenvalues using Eq. (3.13).

Since the fourth-order accurate discretization uses two node points, any arbitrary distribution of node points may be used in order to cluster points in the critical layer. Here we used the distribution of points given by

$$y = y_i(1 - \cos \pi \eta)/2; \quad 0 \leq \eta \leq 1 \quad (3.18)$$

and

$$y = y_i + \frac{a\eta}{b - \eta}; \quad \eta > 1, \quad (3.19)$$

where

$$b = 1 + a/(y_{\max} - y_i)$$

and

$$a = y_o - y_i,$$

where y_o is chosen to give the appropriate distribution of points. In the present study, it was taken to be the location of the edge of the thermal boundary layer defined as $T_e/T = 0.99$. One-half of the total node points are used in the region $y < y_i$.

Single Domain Spectral (SDSP) Collocation Method

The implementation of a spectral algorithm based upon collocation is almost as straightforward as the finite-difference scheme once the derivative matrices are set up. The use of collocation also simplifies the treatment of boundary conditions and coordinate transformations. We use N th order Chebyshev polynomials T_N defined on the interval $-1 \leq \xi_j \leq 1$, where the collocation points ξ_j are the extrema of T_N and are given as

$$\xi_j = \cos \frac{\pi j}{N}; \quad j = 0, 1, \dots, N. \quad (3.20)$$

In order to apply the spectral collocation method, an interpolant polynomial is constructed for the dependent variables in terms of their values at the collocation points. Thus an N th order polynomial may be written as

$$\phi(\xi) = \sum_{k=0}^N \lambda_k(\xi) \phi(\xi_k), \quad (3.21)$$

where the interpolant $\lambda_k(\xi)$ for the Chebyshev scheme is given as

$$\lambda_k(\xi) = \left(\frac{1 - \xi_k^2}{\xi - \xi_k} \right) \frac{T'_N(\xi)}{N^2 c_k} (-1)^{k+1}, \quad (3.22)$$

where

$$c_0 = c_N = 2 \quad \text{and} \quad c_k = 1, \quad 0 < k < N.$$

The first derivative of $\phi(\xi)$ may be written as

$$\left. \frac{d\phi}{d\xi} \right|_j = \sum_{k=0}^N E_{jk} \phi_k, \quad (3.23)$$

where E_{jk} are the elements of the derivative matrix given as [15]

$$\begin{aligned} E_{jk} &= \frac{c_j}{c_k} \frac{(-1)^{k+j}}{\xi_j - \xi_k}; \quad j \neq k \\ E_{jj} &= -\frac{\xi_j}{2(1 - \xi_j^2)} \\ E_{00} &= \frac{2N^2 + 1}{6} = -E_{NN}. \end{aligned}$$

If the scaling factor for the transformation between physical and computational domains is given as

$$S_j = \partial \xi / \partial y |_j; \quad j = 0, 1, \dots, N,$$

then the first derivative matrix F in the physical domain may be written as

$$F_{jk} = S_j E_{jk} \quad (3.24)$$

and the second derivative matrix G_{jk} is simply

$$G_{jk} = F_{jm} F_{mk}. \quad (3.25)$$

Now the governing equation (2.32) may be written at the collocation points ξ_j as

$$A_j \sum_{k=0}^N G_{jk} \phi_k + B_j \sum_{k=0}^N F_{jk} \phi_k + C_j \phi_j = 0. \quad (3.26)$$

We use the boundary conditions given by Eqs. (2.33)–(2.34) at $y=0$ and $y=y_{\max}$. In addition, we use Neumann conditions on pressure as

$$\left. \frac{\partial \hat{p}}{\partial y} \right|_{y=0} = \chi_0 \quad (3.27)$$

$$\left. \frac{\partial \hat{p}}{\partial y} \right|_{y=y_{\max}} = \chi_m, \quad (3.28)$$

where χ_0 and χ_m are prescribed by evaluating the normal momentum equation at the two boundaries. The extra boundary conditions are needed because we have not used a staggered grid as used for the 2FD scheme. Now, Eqs. (3.26)–(3.28) may be represented as

$$\bar{A}\phi = \omega \bar{B}\phi, \quad (3.29)$$

where the vector ϕ contains $5N-3$ elements

$$\{(\hat{u}_j, \hat{v}_j, \hat{p}_j, \hat{T}_j, \hat{w}_j)_{j=1, N-1}, \hat{p}_0, \hat{p}_N\}^T$$

and \bar{A} is a square matrix of order $5N-3$. Since the boundary conditions (3.27)–(3.28) do not contain the eigenvalue ω , \bar{B} is singular. The singularity is removed through column operations and the order of the matrices is reduced to $5(N-1)$. A standard eigenvalue subroutine may now be used to compute $5(N-1)$ eigenvalues.

Both the algebraic and exponential stretchings may be employed to transform the physical domain $0 \leq y \leq y_{\max}$ to the computational domain $-1 \leq \xi \leq 1$. However, algebraic stretchings are more robust for spectral methods. We employ the stretching

$$y = a \frac{1 + \xi}{b - \xi}, \quad (3.30)$$

where $b = 1 + 2a/y_{\max}$ and $a = y_i y_{\max}/(y_{\max} - 2y_i)$. Here y_i is the location corresponding to $\xi = 0$, i.e., half the grid points are located in the region $0 \leq y \leq y_i$.

The mapping given above clusters grid points near the wall. In high Mach number flows one also needs better resolution near the edge of the boundary layer.

While other mappings may be designed to cluster points near the edge of the boundary layer, we consider a multi-domain spectral collocation method which may be used to cluster points in the interior of the physical domain. The multi-domain methods will also prove advantageous if there exist multiple regions of instability, in which case a number of domains could be used to resolve the critical layers.

Multi-Domain Spectral (MDSP) Collocation Method

In recent years, multi-domain spectral methods have become fashionable for fluid mechanics problems (see, e.g., [16–17]). Here we use this approach for eigenvalue problems. The method is described here for two domains but the same technique may be used to construct the algorithm for three or more domains.

The physical domain $0 \leq y \leq y_{\max}$ is divided into two domains $0 \leq y \leq y_i$ and $y_i \leq y \leq y_{\max}$ which may be denoted as domain I and domain II, respectively. The governing equation (2.32) now may be written in the two domains as

$$AD_1^2 \phi^I + BD_1 \phi^I + C\phi^I = 0; \quad 0 \leq y \leq y_i \quad (3.31)$$

$$AD_{II}^2 \phi^{II} + BD_{II} \phi^{II} + C\phi^{II} = 0; \quad y_i \leq y \leq y_{\max} \quad (3.32)$$

with the boundary conditions

$$\phi_1^I = \phi_2^I = \phi_4^I = \phi_5^I = 0; \quad y = 0 \quad (3.33)$$

$$\phi_1^{II} = \phi_2^{II} = \phi_4^{II} = \phi_5^{II} = 0; \quad y = y_{\max} \quad (3.34)$$

and

$$\left. \frac{d\phi_3^I}{dy} \right|_{y=0} = \chi_0, \quad (3.35)$$

$$\left. \frac{d\phi_3^{II}}{dy} \right|_{y=y_{\max}} = \chi_m \quad (3.36)$$

as in (3.27) and (3.28) above.

In addition we need interface conditions at $y = y_i$. These are provided by requiring the continuity of all the elements of ϕ at $y = y_i$, i.e.,

$$\phi^I|_{y=y_i} = \phi^{II}|_{y=y_i}. \quad (3.37)$$

We further require that

$$\left. \frac{d\phi^I}{dy} \right|_{y=y_i} = \left. \frac{d\phi^{II}}{dy} \right|_{y=y_i}. \quad (3.38)$$

We will comment on this requirement later. In Eqs. (3.37)–(3.38), we have 10 conditions that must be satisfied at the interface.

The physical domains $0 \leq y \leq y_i$ and $y_i \leq y \leq y_{\max}$ are now transformed to the

nonzero elements are indicated by $e, f, i, b, c, 1$, and 2 . The index i denotes the fact that these elements have contributions from both the domains. The entries $e, 1, b$ have contributions only from domain 1 while the entries $f, 2, c$ have contributions only from domain 2. The middle five and the last two rows represent the interface conditions and the pressure boundary conditions, respectively. Though this structure was independently derived, it is quite similar to the one used by Hirsch and Gottlieb [18] for a model problem. The matrix \bar{B} is singular since pressure boundary conditions and the interface conditions do not contain the eigenvalue ω . The singularity is removed by row and column operations and, in the process, the order of the system reduces to $5(N1 + N2 - 2)$. The $5(N1 + N2 - 2)$ eigenvalues are obtained by the standard approach mentioned above.

The condition of continuity of fluxes imposed by Eq. (3.38) may be relaxed to allow some jump in the flux to balance a suitable combination of the residual of the discretized equation from both domains as suggested by Quarteroni and Sacchi-Landriani [19]. This particularly makes sense when the stretchings used in the two domains are discontinuous at the interface and when different resolutions are used in the two domains. Another possibility that we have not explored is using a staggered grid as used for the 2FD scheme. In the present context of a multi-domain spectral method, all the second-order equations will be enforced at the collocation points

$$\xi_j^I = \cos \frac{\pi j}{N1}; \quad j = 1, 2, \dots, N1 - 1$$

in domain I, and

$$\xi_j^{II} = \cos \frac{\pi j}{N2}; \quad j = 1, 2, \dots, N2 - 1$$

in domain II. The velocity components $\hat{u}, \hat{v}, \hat{w}$ and temperature \hat{T} will also be defined at these points. The continuity equation will be enforced at

$$\xi_{j+1/2}^I = \cos \frac{\pi(j+1/2)}{N1}; \quad j = 0, 1, \dots, N1 - 1$$

in domain I, and

$$\xi_{j+1/2}^{II} = \cos \frac{\pi(j+1/2)}{N2}; \quad j = 0, 1, \dots, N2 - 1$$

in domain II. The pressure will also be defined at these points. The use of staggered mesh eliminates the need for pressure boundary conditions (3.35)–(3.36). More importantly, no interface conditions for pressure are required. The staggered grid has been used by Macaraeg, Streett, and Hussaini [20] for high speed flows. In the context of a single domain spectral method, it was used by Malik, Zang, and

Hussaini [21] for incompressible Navier–Stokes equations. Recently, Khorrami [22] has used it for a vortex stability problem.

If a guess for the temporal eigenvalue is available then one can improve its value by a local method. The inverse Rayleigh iteration procedure [14] is one such method which yields cubic convergence. The generalization of this procedure to compressible stability eigenvalue problem (3.29) results in the following algorithm:

$$(\bar{A} - \omega_j \bar{B})\phi^{(k+1)} = \bar{B}\phi^{(k)} \quad (3.41)$$

$$(\bar{A} - \omega_j \bar{B})^{\text{tr}} \phi^{\dagger(k+1)} = \bar{B}^{\text{tr}} \phi^{\dagger(k)}. \quad (3.42)$$

The iteration cycle is started with a guessed eigenvalue ω_0 and by assuming any smooth functional distribution for the eigenfunction $\phi^{(0)}$ and its adjoint $\phi^{\dagger(0)}$. For some problems, we have also tried random numbers for the guess $\phi^{(0)}$ and $\phi^{\dagger(0)}$ and still the converged solution was obtained. Two iteration loops are involved in this algorithm. The inner iteration denoted by index k is performed for a fixed ω_j starting with $j=0$. The solution to Eq. (3.41)–(3.42) is obtained and at the end of each iteration cycle k the eigenfunction and its adjoint are normalized so that

$$\phi^{(k+1)} = \phi^{(k+1)} / \max(\phi^{(k+1)}) \quad (3.43)$$

$$\phi^{\dagger(k+1)} = \phi^{\dagger(k+1)} / \max(\phi^{\dagger(k+1)}). \quad (3.44)$$

Once a converged solution for $\phi^{(k+1)}$ and $\phi^{\dagger(k+1)}$ is achieved, the new eigenvalue may be calculated as

$$\omega_{j+1} = \frac{(\phi^{\dagger}, \bar{A}\phi)}{(\phi^{\dagger}, \bar{B}\phi)}, \quad (3.45)$$

where the inner product is the usual L_2 vector inner product.

The iteration k may now be repeated. Depending upon the initial guess for the eigenvalue and eigenfunctions, it takes 4 to 10 inner iterations to achieve a converged solution for the eigenfunctions. A converged eigenvalue is obtained in two or at worst in three outer iterations j .

An alternative to the inverse Rayleigh iteration procedure is to use Eq. (3.13) as for the 4CD scheme. This has the advantage that spatial eigenvalues may also be obtained with the same amount of computational effort as for the temporal problem. This will be discussed in Section 5 below.

4. TEMPORAL STABILITY RESULTS

Now we present the results of our calculations to test the performance and accuracy of the various numerical schemes discussed above. The test cases are described in Table I, where the flow Mach number (M), Reynolds number (R), the ratio of wall temperature to adiabatic wall temperature (T_w/T_{adb}), stagnation tem-

TABLE I
Description of Test Cases

Test case	Mach number	R	T_w/T_{adb}	T_0 0R	δ^*	y_i
1	0.5	2000	1	500	1.8236	3
2	10^{-6}	580	1	500	1.7208	3
3	2.5	3000	1	600	4.2578	6
4	10.0	2000	0.1	4200	12.917	13
5	10.0	1000	1	4200	31.679	32
6	4.5	1500	1	1100	9.3992	11

perature (T_0), and nondimensional (scaled with ℓ) displacement thickness δ^* are presented. The length scale ℓ is taken to be $\ell = \sqrt{\nu_e x / u_e}$, where ν_e is the kinematic viscosity at the boundary layer edge temperature. For hypersonic boundary layers, the displacement thickness approaches the boundary layer thickness and the critical layer for the most amplified mode lies in close proximity to these thicknesses. Also presented in the table is the parameter y_i as described in Eq. (3.19) and Eqs. (3.31)–(3.32).

First, results for the Mach 0.5 case are presented in Table II. The wave number α is 0.1, and the Reynolds number is 2000. The performance of 2FD scheme is consistent with second-order accuracy of the method. The unstable mode is captured using only 17 nodes, though the growth rate is almost 50% lower than the desired value. However, this is not a serious drawback since the purpose of the global method here is to provide a guess of the eigenvalue for local computations using the fourth-order scheme. Indeed, this value for $N=16$ is used as a guess for all the eigenvalues computed using the 4CD scheme presented in the table. Five-digit accuracy with this scheme is achieved with 33 node points as compared to the results of the SDSP scheme which takes only 25 nodes to achieve the same

TABLE II
Real and Imaginary Parts of the Eigenvalue ω for Test Case Number 1, $\alpha=0.1$, $\beta=0$

$N+1$	2FD		4CD		SDSP		MDSP	
17	0.029659	0.001338	0.0290542	0.0022046	0.02917687	0.00230046	0.02983413	0.00393174
25	0.029329	0.001819	0.0290777	0.0022342	0.02908247	0.00224387	0.02907451	0.00224283
33	0.029216	0.002002	0.0290841	0.0022413	0.02908189	0.00224427	0.02907808	0.00224400
41	0.029166	0.002088	0.0290835	0.0022430	0.02908185	0.00224419	0.02908167	0.00224419
45	0.029151	0.002115	0.0290825	0.0022434	0.02908180	0.00224419	0.02908173	0.00224418
51	0.029135	0.002144	0.0290822	0.0022437				
61	0.029118	0.002174	0.0290821	0.0022439				
81			0.0290819	0.0022441				

accuracy. For this low Mach number case, the SDSP scheme seems to be better than the MDSP scheme, since the critical layer is still near the wall and multi-domain calculation offers no advantage. Furthermore, we have not experimented with the location of the interface to obtain the optimum results for the MDSP scheme. All of the MDSP results described in this paper were obtained using $N_1 = N_2$. In any case, six-digit accuracy is achieved with 33, 41, and 81 nodes for the SDSP, MDSP, and 4CD schemes, respectively. However, the computational time for the 4CD scheme (including the time taken to obtain the guess from the 2FD scheme) is considerably lower than the time taken by spectral schemes for comparable accuracy. Unless otherwise mentioned, all the results presented in this paper have been obtained by using $y_{\max} = 500$ for the 4CD scheme and $y_{\max} = 100$ for the 2FD, SDSP, and MDSP schemes.

In order to show the order of accuracy of the various schemes, the results of Table II are also presented in Fig. 2 where the error in the eigenvalue is plotted as a function of N . The exact value was assumed to be $0.02908177 + 0.002244185i$ which was obtained from the two spectral schemes. The 2FD scheme is accurate to second order, the 4CD scheme is accurate to about fourth order, and the spectral schemes converge faster. The accuracy of the 2FD scheme may be increased by using the Richardson extrapolation. This was done by Malik and Orszag [6] within the context of local methods. However, in cases where eigenvalue convergence may not be monotonic, extrapolation could produce inferior results.

As discussed earlier, Eq. (3.8) allows \bar{B} in (3.4) to be inverted by using standard block-tridiagonal solvers. An LR solver can then be used to obtain the eigenvalues of $\bar{B}^{-1}\bar{A}$. Alternatively, the actual boundary conditions (3.7) can be used and the generalized eigenvalue problem (3.4) can be solved by using the QZ algorithm. This was done for test case number 1. Except for the eigenvalues associated with (3.8),

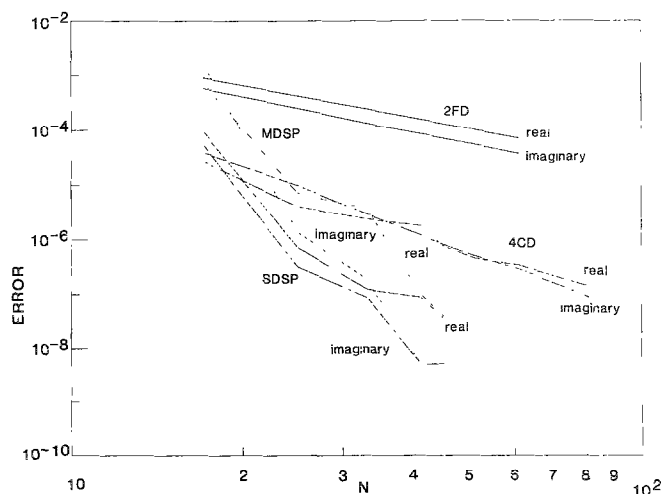


FIG. 2 Absolute error in the real and imaginary parts of the eigenvalue ω for test case number 1.

both approaches produced the same eigenvalues. However, the solution with the QZ algorithm required 60% more computer time.

One advantage of the global method is that the whole spectrum of eigenvalues may be obtained. The spectral schemes described in this paper may be used to study the eigenvalue spectrum of the compressible linear stability problem. This will be done in a later paper for supersonic boundary layers. The temporal eigenvalue spectrum for the Orr–Sommerfeld equation has been studied by several authors (see, e.g., [23]). Here we give some results of the MDSP scheme for the compressible equations but in the limit of Mach number approaching 0 to simulate the Orr–Sommerfeld results. Calculations were actually done for $M = 10^{-6}$ and $R = 580$. Some of the computed eigenvalues are compared with the results of Mack [23] in Table III, where the real and imaginary parts of the computed phase velocity ($c = \omega/\alpha$) are presented.

We note that our results simulate fairly well the Orr–Sommerfeld results computed by Mack [23]. However, there is an additional mode which is less stable than the second Orr–Sommerfeld mode. This mode was first computed by the author's COSAL code [24] which utilizes the 2FD scheme. In that computer code, a local eigenvalue search procedure based on the 2FD discretization and the inverse Rayleigh iteration procedure are also included. The local eigenvalue search using higher resolution also converged for this new mode. However, the 4CD scheme as described above failed to converge for this mode. The obvious question arose whether this mode is physical or not? A careful look at the eigenfunction computed by COSAL code revealed that the mode had produced large temperature perturbations and very little associated velocity perturbations, implying that this mode is an eigenvalue of the energy equation. Knowing this, Eq. (3.13) in the 4CD scheme was replaced by

$$\psi_5(0) + \frac{\partial \psi_5(0)}{\partial \omega} \Delta \omega = 0. \quad (4.1)$$

A converged eigenvalue was then obtained as in Table III. The computed

TABLE III

Comparison of First 5 Modes (Phase Velocity) of the Compressible Stability Equations in the Incompressible limit ($M = 10^{-6}$) with the Orr–Sommerfeld Modes Computed by Mack [23]

$c = \omega/\alpha$			
MDSP		Orr–Sommerfeld modes	
0.3641	0.0079	0.3641	0.0080
0.2329	−0.1343	—	—
0.2897	−0.2768	0.2897	−0.2769
0.4839	−0.1921	0.4839	−0.1921
0.5571	−0.3655	0.5572	−0.3653

Note. $\alpha = 0.179$, $\beta = 0$, $R = 580$.

eigenfunction for this mode along with the first two Orr–Sommerfeld modes are presented in Fig. 3. There would, of course, be a whole family of discrete eigenvalues of the energy equation. What relevance these modes of the energy equation may have in compressible boundary layer transition might be worth exploring.

Next, we test the schemes for higher Mach numbers. First, the results for a Mach 2.5 boundary layer are presented in Table IV. The calculation is made for $\alpha = 0.06$ and $\beta = 0.1$. Now the performance of the MDSP is better than that of the SDSP scheme. The results of the 4CD scheme using $N = 25$ are better than those of the MDSP scheme using the same resolution. This is not uncommon when the results of finite-difference and spectral methods are compared. For any given problem, there is a minimum resolution needed before spectral convergence is achieved. The global calculations using the 2FD and MDSP schemes do not yield any spurious

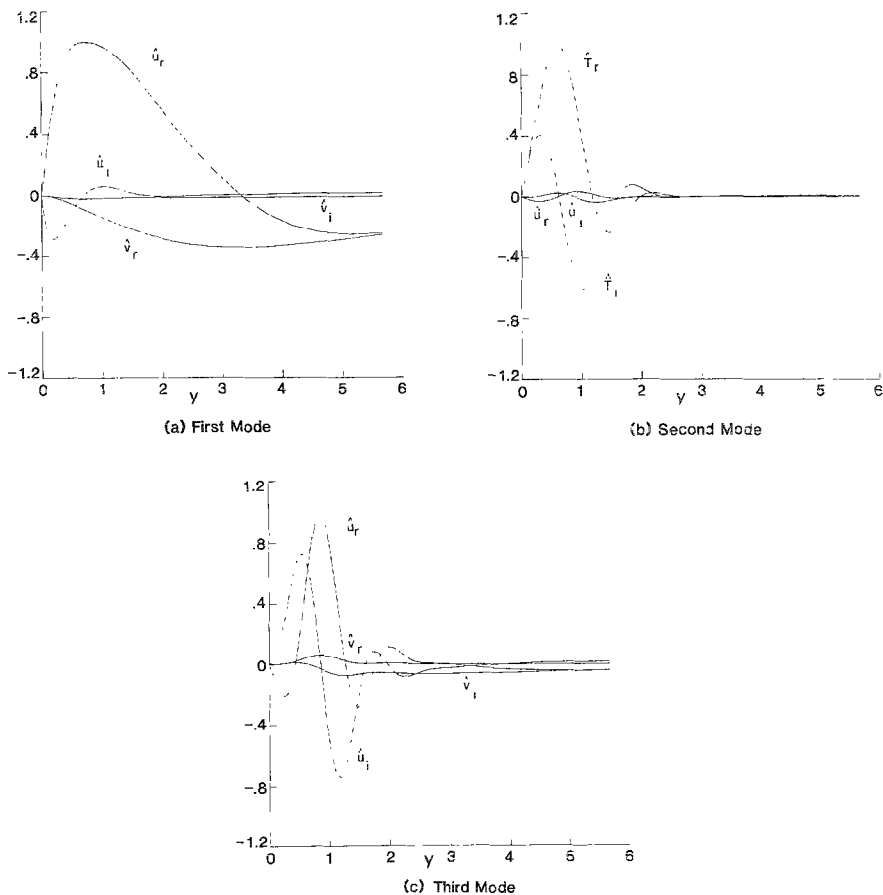


FIG. 3. Eigenfunctions for some of the modes of the compressible stability equations for $M = 10^{-n}$, $R = 580$, $\alpha = 0.179$, $\beta = 0$. The first and third modes are also the modes of the Orr–Sommerfeld equation. The second mode results due to energy equation.

TABLE IV

Real and Imaginary Parts of the Eigenvalue ω for Test Case Number 3, $\alpha = 0.06$, $\beta = 0.1$

$N+1$	2FD		4CD		SDSP		MDSP	
25	0.0369069	0.0006007	0.0367075	0.0005842	0.0368934	0.0004199	0.0369488	0.0003527
33	0.0368173	0.0005478	0.0367195	0.0005866	0.0366808	0.0006584	0.0367264	0.0005710
41	0.0367885	0.0005604	0.0367265	0.0005855	0.0367521	0.0005865	0.0367332	0.0005847
51	0.0367689	0.0005687	0.0367300	0.0005851	0.0367332	0.0005832	0.0367340	0.0005840
61	0.0367583	0.0005733	0.0367321	0.0005847	0.0367339	0.0005840	0.0367340	0.0005840

unstable modes. However, the present formulation of the SDSP scheme yields an additional unstable mode. Spurious unstable modes are not uncommon in global calculations [25] and special care has to be taken to eliminate these modes. Perhaps, a staggered formulation of the SDSP scheme will cure the problem.

Test case number 4 pertains to a calculation of the second mode [3] at a Mach number of 10. Compressible boundary layers have a generalized inflection point defined by $d/dy(\rho dU/dy) = 0$. The presence of this inflection point is a sufficient condition for instability. The Mach 2.5 calculation performed above shows an instability due to the presence of such a generalized inflection point. This is often called the first mode of instability. This mode is most unstable for oblique waves and is stabilized by wall cooling, favorable pressure gradient, and wall suction. At Mach numbers above about 4, there are additional modes which, for their existence, do not require the presence of a generalized inflection point. The first of these modes is generally the most unstable one and dominates boundary layer transition at high Mach numbers [3, 26]. This mode has the highest growth rate when the wave-angle is zero and cannot be stabilized with wall cooling. In fact, wall cooling has a destabilizing effect on this mode. It is this mode that is being computed in test case number 4 with a wall to adiabatic wall temperature ratio of 0.1, $\alpha = 0.105$, and $R = 2000$. The eigenfunctions for this mode are presented in Fig. 4. While the peak

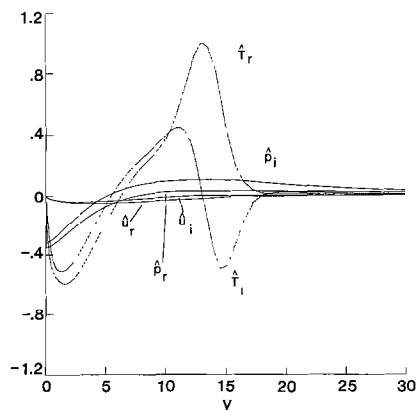


FIG. 4. Disturbance eigenfunctions for a hypersonic boundary layer, $M = 10$, $R = 2000$, $T_w/T_{adb} = 0.1$, $\alpha = 0.105$, $\beta = 0$.

TABLE V

Real and Imaginary Parts of the Eigenvalue ω for Test Case Number 4, $\alpha=0.105$, $\beta=0$

$N+1$	2FD		4CD		SDSP		MDSP	
25	0.0971936	0.0022453	0.0974114	0.0020600	0.0969286	0.0020306	0.0976239	0.0019983
33	0.0971538	0.0019907	0.0974615	0.0019927	0.0974286	0.0018622	0.0974575	0.0020671
41	0.0973031	0.0019763	0.0974765	0.0020341	0.0975555	0.0020086	0.0974995	0.0020129
51	0.0973671	0.0020122	0.0974823	0.0020308	0.0974858	0.0020526	0.0974802	0.0020328
61	0.0974002	0.0020224	0.0974832	0.0020308	0.0974774	0.0020302	0.0974864	0.0020316
81			0.0974837	0.0020304				

of the temperature perturbation lies near the edge of the boundary layer, it is not very sharp and this mode is well captured by all the schemes. The results of these calculations are presented in Table V. The 2FD scheme provides a very good guess for the eigenvalue even with $N=25$. The 4CD scheme provides five-digit accuracy with 51 node points. The MDSP scheme provides five-digit accuracy with the same number of node points. The performance of the SDSP scheme is somewhat poor as only four-digit convergence is achieved. The eigenvalue oscillates in the fifth digit. This may be explained by the resolution provided by the two spectral schemes in the neighborhood of $y = y_i$ ($\xi = 0$) as depicted in Fig. 5. The SDSP scheme provides the highest resolution near the wall and then it steadily deteriorates away from the wall. The MDSP scheme provides relatively less resolution near the wall but provides more resolution near $\xi = 0$.

A much more severe test for the various schemes is provided in Table VI, where results are presented for test case number 5. The wall temperature is now adiabatic, Mach number is 10, $\alpha=0.12$, and $R=1000$. The parameters chosen are such that they produce a mode whose eigenfunction consists of a very sharp peak in temperature perturbation near the boundary layer edge. The relative magnitude of velocity fluctuations is very small as shown in Fig. 6. The performance of the 4CD

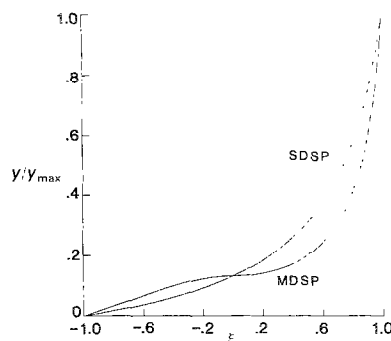


FIG. 5. Comparison of resolution provided by SDSP and MDSP scheme for the same total node points.

TABLE VI
Real and Imaginary Parts of the Eigenvalue ω for Test Case Number 5, $\alpha=0.12$, $\beta=0$

$N+1$	2FD		4CD		SDSP		MDSP	
25	0.1163679	0.0014440	0.1157999	-0.0000071	0.1145183	0.0009373	0.1157335	-0.0002989
33	0.1158070	0.0009287	0.1158523	0.0001842	0.1147691	0.0007327	0.1158719	0.0001094
41	0.1157499	0.0004592	0.1158613	0.0001416	0.1150698	0.0001450	0.1159041	0.0001143
51	0.1159275	0.0003503	0.1158590	0.0001496	0.1155532	0.0003080	0.1158529	0.0001999
61	0.1158706	0.0003251	0.1158630	0.0001521	0.1161434	-0.0001949	0.1158519	0.0001357
81			0.1158647	0.0001529				

scheme is again excellent with five-digit convergence provided by 61 nodes. Due to second-order accuracy, the convergence of the 2FD scheme is slow but consistent. For this test case, the 4CD scheme did not converge for the guess provided by the 25-node solution with the 2FD scheme. However, it converged with the guess provided by the 33-node solution using the 2FD scheme.

The performance of the SDSP scheme is quite poor as the eigenvalue oscillates; with a 61-node solution indicating no instability while the 4CD scheme gives the growth rate to be 0.0001529. The performance of the MDSP scheme is better but not completely satisfactory as there are some oscillations in the eigenvalue. These oscillations, perhaps, could be controlled with an improved treatment of the interface as discussed above. Even for this case, both the 2FD and MDSP schemes only give one unstable mode and no spurious unstable modes. One of the reviewers of this paper used his IVM code (4th-order Runge-Kutta) to compute this mode using 100 integration steps. With the 2FD eigenvalue for $N=24$ as the guess, there was no convergence; with $0.116 + 0.00015i$, there was. Starting the integration at $y=39.6$, he got the eigenvalue $0.1158627 + 0.0001557i$; starting at 37.5, he got $0.1158644 + 0.0001539i$.

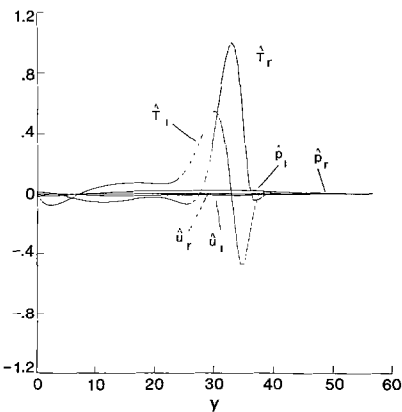


FIG. 6. Disturbance eigenfunction for a hypersonic boundary layer, $M=10$, $R=2000$, adiabatic wall, $\alpha=0.12$, $\beta=0$.

5. EXTENSION TO SPATIAL STABILITY

The spatial eigenvalue α appears nonlinearly in the governing equations (2.32) so they are not directly amenable to global analysis using the generalized eigenvalue approach. As discussed by Khorrami, Malik, and Ash [12], one alternative is to consider the transformation

$$\begin{aligned}\tilde{u} &= \alpha \hat{u} \\ \tilde{v} &= \alpha \hat{v} \\ \tilde{T} &= \alpha \hat{T} \\ \tilde{w} &= \alpha \hat{w}.\end{aligned}\tag{5.1}$$

This allows Eqs. (2.32)–(2.34) to be set up as a generalized eigenvalue problem, where the solution vector now contains nine elements:

$$\phi = \{\hat{u}, \hat{v}, \hat{p}, \hat{T}, \hat{w}, \tilde{u}, \tilde{v}, \tilde{T}, \tilde{w}\}^T.\tag{5.2}$$

For an N node discretization, the order of the matrices involved is $9N$ and the computational cost for the global solution is of $O((9N)^3)$. This is certainly a high cost over the temporal solution, where the order of the matrices was $5N$ for three-dimensional disturbances.

The nonlinearity in α arises from the viscous (\hat{u}_{xx}) terms. Since the instability in high Mach number flows is inviscid in nature, the contribution from the viscous terms should be relatively small. The idea is to drop the α^2 term in a global eigenvalue search since this is only done to provide a guess for the higher resolution local calculations. With this approximation, the global calculations may be made with the same demands on computer resources as for a temporal search. Thus, the generalized eigenvalue problem is set up for spatial stability as

$$\bar{A}\phi = \alpha\bar{B}\phi.\tag{5.3}$$

For the 2FD scheme, \bar{B} is block-tridiagonal and nonsingular. Therefore, $\bar{B}^{-1}\bar{A}$ may be constructed using a block-tridiagonal solver. For the MDSP scheme, \bar{B} is made nonsingular as for the temporal problem. For the same N , the solution for the 2FD scheme may be obtained for substantially less computational cost as compared to the solution by the MDSP scheme. Furthermore, the memory requirements are roughly half.

The spatial stability results for the 2FD and MDSP schemes are compared in Table VII for a Mach number of 4.5, $\omega = 0.23$, and $R = 1500$ (test case number 6). The MDSP scheme performs quite well for the spatial stability. For $N = 32$, the CPU time for the two schemes (with the approximation $\alpha^2 = 0$) is given in Table VIII. For comparison, the time for the 4CD scheme is also given. The guess for the 4CD calculation was provided by an $N = 24$ calculation using the 2FD scheme.

TABLE VII
Spatial Eigenvalue α for Test Case Number 6, $\omega = 0.23$, $\beta = 0$

$N + 1$	2FD		MDSP	
25	0.2490059	-0.0051672	0.2537500	-0.0030012
33	0.2535164	-0.0052589	0.2533568	-0.0029078
41	0.2546765	-0.0035031	0.2533264	-0.0028657
51	0.2535841	-0.0032119	0.2534592	-0.0028893
61	0.2536248	-0.0030988	0.2534081	-0.0028860

Note. The approximation $\alpha^2 = 0$ has been made.

While the computational time increases linearly with N for the 4CD scheme, it varies as N^3 for global calculations using 2FD and MDSP schemes.

Since the 4CD scheme uses a local method, the spatial eigenvalue solution may be obtained without the approximation $\alpha^2 = 0$. For the spatial eigenvalue α , Eq. (3.13) and (3.14) are replaced by

$$\psi_1(0) + \frac{\partial \psi_1(0)}{\partial \alpha} \Delta \alpha = 0 \quad (5.4)$$

and

$$L \frac{\partial \Psi}{\partial \alpha} = - \frac{\partial L}{\partial \alpha} \Psi. \quad (5.5)$$

Thus, this solution is obtained in the same time as for the temporal problem using block-tridiagonal inversions. For local eigenvalue problems, the MDSP scheme can also be used to obtain α by using Eqs. (5.4)–(5.5) without requiring the approximation $\alpha^2 = 0$ needed above for the global problem. We have done so again for the Mach 4.5 test case and the results are presented in Table IX. Five-digit agreement between the two schemes is achieved with 61 nodes for the MDSP scheme and 81 nodes for the 4CD scheme. Here, our purpose was simply to demonstrate the spatial local eigenvalue solution capability of the MDSP scheme. We believe that its performance could be improved by imposing asymptotic boundary conditions in

TABLE VIII
Execution Time on Cyber 860 Computer for Spatial Eigenvalue
Calculation for Test Case Number 6

Scheme	Time (s)
2FD	32
4CD	2
MDSP	76

Note. Using $N = 32$.

TABLE IX
Spatial Eigenvalue α for Test Case Number 6, $\omega = 0.23$, $\beta = 0$

$N + 1$	4CD		MDSP	
25	0.2536404	-0.0023801	0.2549472	-0.0004127
33	0.2534544	-0.0024718	0.2529197	-0.0022167
41	0.2534276	-0.0024856	0.2533691	-0.0025075
51	0.2534168	-0.0024917	0.2533993	-0.0024912
61	0.2534120	-0.0024933	0.2534048	-0.0024921
81	0.2534081	-0.0024932		

Note. MDSP calculations performed using the local method.

the free-stream at a smaller distance from the wall. In the present example, we imposed zero perturbation boundary conditions at $y=100$ as for the global method. The performance of the 4CD scheme may also be improved in a similar fashion.

A comparison of the results in Table VII and Table IX indicates the order of error incurred due to the approximation $\alpha^2=0$. While the real part of the eigenvalue is the same up to four digits, the imaginary part (growth rate) is in error by about 0.0004. This amounts to a 15% error in the growth rate. In percentage terms, this error will be even larger near the neutral curve. However, the purpose of the approximation is to provide a "cheap guess" for the spatial local calculations. The author has performed a number of calculations at various Mach numbers ranging from about 0.8 to 10 and this approximation serves its purpose. The alternative, of course, is to pay almost six times higher computational cost. Of course, if the complete global eigenvalue spectrum is required, the full 9th-order system (see Eq. (5.2)) may be solved. In Ref. [12], the full system for the incompressible problem was solved.

It is worth mentioning that both of the local methods compared in Table IX could be used to generate neutral curves or curves of constant growth. If, for example, the locus of $\omega_i = \alpha_i = 0$ is sought then given an initial guess for α_r and ω_r , the corrections $\Delta\alpha_r$ and $\Delta\omega_r$ may be determined from the equations

$$\psi_{1r}(0) + \frac{\partial\psi_{1r}(0)}{\partial\alpha_r} \Delta\alpha_r + \frac{\partial\psi_{1r}(0)}{\partial\omega_r} \Delta\omega_r = 0$$

$$\psi_{1i}(0) + \frac{\partial\psi_{1i}(0)}{\partial\alpha_r} \Delta\alpha_r + \frac{\partial\psi_{1i}(0)}{\partial\omega_r} \Delta\omega_r = 0.$$

It is less efficient to use an inverse Rayleigh iteration procedure to construct curves of constant growth.

Finally, we show the effect of various stretchings on the spatial eigenvalue computed by the 4CD scheme (see Table X). This calculation is performed for Mach 10 flow at a Reynolds number of 1000 and $\omega = 0.09$. The wall temperature was set

TABLE X
Effect of Various Stretchings on the Eigenvalue α Using 4CD Scheme

$N + 1$	Stretching 1 (Eq. (3.1) with $a = \delta^*$)	Stretching 2 (Eq. (3.1) with $a = \delta^* y_{\max} / (y_{\max} - 2 \delta^*)$)	Stretching 3 (Eqs. (3.18)–(3.19))
11	0.095110	0.004124	0.097082
21	0.095830	–0.002312	–0.002776
31	0.096020	–0.002175	–0.001716
41	0.095962	–0.002142	0.095985
51	0.095943	–0.002152	–0.002177
61	0.095938	–0.002155	0.095950
71	0.095936	–0.002156	–0.002144
81	0.095935	–0.002156	0.095950
			–0.002154
			0.095933
			–0.002156
			0.095933
			–0.002156
			0.095933
			–0.002156
			0.095933
			–0.002156

Note. $M = 10$, $R = 1000$, $\omega = 0.09$, $y_{\max} = 100$.

at $2000^\circ R$ while the free stream static temperature was held at $480^\circ R$. In this case $y_{\max} = 100$. Three different stretchings were considered:

1. same as Eq. (3.1) but with $a = \delta^*$.
2. same as Eq. (3.1) with $a = y_{\max} \delta^* / (y_{\max} - 2 \delta^*)$.
3. The stretching given by Eqs. (3.18)–(3.19) with two-thirds of the total node points used in the region $y < y_i$.

The results for α are presented for $N = 10, 20, \dots, 80$. While for sufficiently refined grids all three stretchings give comparable results, the performance of stretching number 3 is superior to other stretchings, particularly for crude mesh. This stretching provides five-digit accuracy at this Mach number for only 31 node points. The imaginary part is converged to six digits for the same resolution.

6. CONCLUDING REMARKS

We have developed and compared four different schemes for the solution of compressible boundary layer stability equations. Both the temporal and spatial stability are considered for a global eigenvalue spectrum and a local eigenvalue search. The discretizations considered include a second-order staggered finite-difference scheme, a fourth-order accurate two-point compact scheme, a single-domain Chebyshev spectral collocation scheme, and a multi-domain spectral collocation scheme. All the schemes perform quite well at low Mach numbers with collocation schemes providing spectral accuracy. A new mode of the compressible stability equations is identified in the limit of vanishing Mach number.

As the Mach number increases, the performance of the single domain spectral

collocation scheme deteriorates due to the outward movement of the critical layer. Therefore, a multi-domain spectral method is designed to provide better resolution of the critical layer. Results are presented for this scheme for temporal global eigenvalue calculations, spatial global eigenvalue calculations, and spatial local eigenvalue calculations. The results are compared with other schemes. The overall performance of the compact difference scheme is excellent with very accurate eigenvalues for less than 81 node points, in general, and very little computer time. The performance of the multi-domain spectral method at high Mach numbers needs to be improved. Perhaps, a different treatment of the interface will yield better convergence.

APPENDIX I

The non-zero elements of the coefficient matrices in Eq. (2.32) for 3D basic flow are given below. For results presented in this paper, set $W' = 0$:

$$B_{11} = \frac{1}{\mu} \frac{d\mu}{dT} T'$$

$$B_{12} = i\alpha l_1$$

$$B_{14} = \frac{1}{\mu} \frac{d\mu}{dT} U'$$

$$B_{21} = i\alpha l_1/l_2$$

$$B_{22} = \frac{1}{\mu} \frac{d\mu}{dT} T'$$

$$B_{23} = -R/(l_2\mu)$$

$$B_{25} = i\beta l_1/l_2$$

$$B_{32} = 1$$

$$B_{41} = 2(\gamma - 1)\sigma M^2 U'$$

$$B_{44} = 2k'/k$$

$$B_{45} = 2(\gamma - 1)\sigma M^2 W'$$

$$B_{52} = i\beta l_1$$

$$B_{54} = \frac{1}{\mu} \frac{d\mu}{dT} W'$$

$$B_{55} = \frac{1}{\mu} \frac{d\mu}{dT} T'$$

$$C_{11} = -i\zeta R/(\mu T) - (l_2\alpha^2 + \beta^2)$$

$$C_{12} = -RU' / (\mu T) + \frac{i\alpha}{\mu} \frac{d\mu}{dT} T'$$

$$C_{13} = -i\alpha R/\mu$$

$$C_{14} = \frac{1}{\mu} \frac{d\mu}{dT} U'' + \frac{1}{\mu} \frac{d^2\mu}{dT^2} T' U'$$

$$C_{15} = -\alpha\beta l_1$$

$$C_{21} = i\alpha \frac{1}{\mu} \frac{d\mu}{dT} T' l_0/l_2$$

$$C_{22} = -i\xi R/(l_2 \mu T) - (\alpha^2 + \beta^2)/l_2$$

$$C_{24} = i \frac{1}{\mu} \frac{d\mu}{dT} (\alpha U' + \beta W')/l_2$$

$$C_{25} = i\beta \frac{1}{\mu} \frac{d\mu}{dT} T' l_0/l_2$$

$$C_{31} = i\alpha$$

$$C_{32} = -T'/T$$

$$C_{33} = i\gamma M^2 \xi$$

$$C_{34} = -i\xi/T$$

$$C_{35} = i\beta$$

$$C_{42} = 2i(\gamma - 1) M^2 \sigma (\alpha U' + \beta W') - \sigma R T' / (\mu T)$$

$$C_{43} = i\xi(\gamma - 1) M^2 \sigma R / \mu$$

$$C_{44} = -i\xi R \sigma / (\mu T) - (\alpha^2 + \beta^2) + (\gamma - 1) M^2 \sigma \frac{1}{\mu} \frac{d\mu}{dT} (U'^2 + W'^2) + k''/k$$

$$C_{51} = -\alpha\beta l_1$$

$$C_{52} = i\beta \left(\frac{1}{\mu} \frac{d\mu}{dT} \right) T' - R W' / (\mu T)$$

$$C_{53} = -i\beta R / \mu$$

$$C_{54} = \frac{1}{\mu} \frac{d\mu}{dT} W'' + \frac{1}{\mu} \frac{d^2\mu}{dT^2} T' W'$$

$$C_{55} = -i\xi R / (\mu T) - (\alpha^2 + l_2 \beta^2)$$

where $(\)' \equiv d/dy$ and

$$\xi = \alpha U + \beta W - \omega$$

$$l_j = j + \lambda/\mu.$$

APPENDIX II

The non-zero elements of the coefficient matrix in Eq. (2.36) for 3D basic flow are given below. For the results presented in this paper, set $W=0$:

$$a_{12} = 1$$

$$a_{21} = i\xi R/(\mu T) + (\alpha^2 + \beta^2)$$

$$a_{22} = -\frac{1}{\mu} \frac{d\mu}{dT} T'$$

$$a_{23} = U' R/(\mu T) - i\alpha l_1 T'/T - i\alpha \frac{1}{\mu} \frac{d\mu}{dT} T'$$

$$a_{24} = i\alpha R/\mu - \alpha l_1 \gamma M^2 \xi$$

$$a_{25} = -\frac{1}{\mu} \frac{d\mu}{dT} U'' - \frac{1}{\mu} \frac{d^2\mu}{dT^2} T' U' + \alpha l_1 \xi/T$$

$$a_{26} = -\frac{1}{\mu} \frac{d\mu}{dT} U'$$

$$a_{31} = -i\alpha$$

$$a_{33} = T'/T$$

$$a_{34} = -i\gamma M^2 \xi$$

$$a_{35} = i\xi/T$$

$$a_{37} = -i\beta$$

$$a_{41} = -i\chi l_2 \alpha T'/T - 2i\chi \alpha \frac{1}{\mu} \frac{d\mu}{dT} T'$$

$$a_{42} = -i\chi \alpha$$

$$a_{43} = -\chi \{ i\xi R/(\mu T) + \alpha^2 + \beta^2 \} + l_2 \chi \left\{ \frac{1}{\mu} \frac{d\mu}{dT} T'^2/T + T''/T \right\}$$

$$a_{44} = -i\chi \gamma M^2 l_2 \left\{ \xi \left(\frac{1}{\mu} \frac{d\mu}{dT} T' + T'/T \right) + \alpha U' + \beta W' \right\}$$

$$a_{45} = i\chi \left[(\alpha U' + \beta W') \left(\frac{l_2}{T} + \frac{1}{\mu} \frac{d\mu}{dT} \right) + \xi \frac{l_2}{\mu} \frac{d\mu}{dT} T'/T \right]$$

$$a_{46} = i l_2 \chi \xi/T$$

$$a_{47} = -i\beta \chi \left[\frac{2}{\mu} \frac{d\mu}{dT} T' + l_2 T'/T \right]$$

$$a_{48} = -i\beta \chi$$

$$a_{56} = 1$$

$$a_{62} = -2(\gamma - 1) M^2 \sigma U'$$

$$a_{63} = -2i(\gamma - 1) M^2 \sigma (\alpha U' + \beta W') + \sigma R T'/(\mu T)$$

$$a_{64} = -i\xi(\gamma - 1) M^2 \sigma R/\mu$$

$$a_{65} = i\xi R\sigma/(\mu T) + (\alpha^2 + \beta^2) - (\gamma - 1) M^2 \sigma \frac{1}{\mu} \frac{d\mu}{dT} (U'^2 + W'^2) - k''/k$$

$$a_{66} = -2k'/k$$

$$a_{68} = -2(\gamma - 1)M^2\sigma W'$$

$$a_{78} = 1$$

$$a_{83} = -i\beta \frac{1}{\mu} \frac{d\mu}{dT} T' - i\beta l_1 T'/T + RW' / (\mu T)$$

$$a_{84} = i\beta R/\mu - \beta l_1 \gamma M^2 \xi$$

$$a_{85} = \beta l_1 \xi / T - \frac{1}{\mu} \frac{d\mu}{dT} W'' - \frac{1}{\mu} \frac{d^2\mu}{dT^2} T' W'$$

$$a_{86} = -\frac{1}{\mu} \frac{d\mu}{dT} W''$$

$$a_{87} = i\xi R/(\mu T) + \alpha^2 + \beta^2$$

$$a_{88} = -\frac{1}{\mu} \frac{d\mu}{dT} T'$$

where, $()' \equiv d/dy$ and

$$\xi = (\alpha U + \beta W - \omega)$$

$$\chi = 1/\{R/\mu + i\gamma M^2 \xi l_2\}$$

$$l_j = j + \lambda/\mu.$$

ACKNOWLEDGMENTS

This work was partly supported by NASA Contract NAS1-18240. The author thanks Mr. Ivan Beckwith and Mr. Dennis Bushnell of NASA Langley for their support. The author also thanks the reviewers for very helpful comments.

REFERENCES

1. L. LEES AND C. C. LIN, "Investigation of the Stability of the Laminar Boundary Layer in a Compressible Fluid," NACA Technical Note No. 1115, 1946 (unpublished).
2. L. M. MACK, "Computation of the Stability of the Laminar Compressible Boundary Layer," in *Methods in Computational Physics*, edited by B. Alder (Academic Press, New York, 1965), Vol. 4, p. 247.
3. L. M. MACK, "Boundary Layer Linear Stability Theory," AGARD Report No. 709, 1984 (unpublished).
4. M. R. SCOTT AND H. A. WATTS, *SIAM J. Numer. Anal.* **14**, 40 (1977).
5. S. A. ORSZAG, *J. Fluid Mech.* **50**, 689 (1971).
6. M. R. MALIK AND S. A. ORSZAG, "Efficient Computation of the Stability of Three-Dimensional Compressible Boundary Layers," AIAA Paper No. 81-1277, 1981 (unpublished).
7. M. R. MALIK, S. CHUANG, AND M. Y. HUSSAINI, *ZAMP* **33**, 189 (1982).
8. T. J. BRIDGES AND P. J. MORRIS, *J. Comput. Phys.* **55**, 437 (1984).
9. T. HERBERT, "Analysis of the Subharmonic Route to Transition in Boundary Layers," AIAA Paper No. 84-0009, 1984 (unpublished).
10. P. R. SPALART, in *Proc. 9th Int. Conf. Numerical Methods in Fluid Dynamics*, edited by J. P. Boujot and Soubbarameyer, (Springer-Verlag, Berlin/Heidelberg, 1985), p. 531.

11. J. S. BRAMLEY, *J. Comput. Phys.* **64**, 258 (1986).
12. M. R. KHORRAMI, M. R. MALIK, AND R. L. ASH, "Application of Spectral Collocation Techniques to the Stability of Swirling Flows," *J. Comput. Phys.* **81**, 206 (1989).
13. T. CEBECI AND A. M. O. SMITH, *Analysis of Turbulent Boundary Layers* (Academic Press, New York, 1974).
14. J. H. WILKINSON, *The Algebraic Eigenvalue Problem* (Oxford Univ. Press, London, 1965).
15. D. GOTTLIEB, M. Y. HUSSAINI, AND S. A. ORSZAG, "Theory and Applications of Spectral Methods," *Spectral Methods for Partial Differential Equations*, edited by R. G. Voigt, D. Gottlieb, M. Y. Hussaini (SIAM-CBMS, Philadelphia, 1984), p. 1.
16. A. T. PATERA, *J. Comput. Phys.* **54**, 468 (1984).
17. M. G. MACRAEG AND C. L. STREETT, *Appl. Num. Math.* **2**, 95 (1986).
18. D. GOTTLIEB AND R. S. HIRSH, "Parallel Pseudospectral Domain Decomposition Techniques." NASA CR-181629, 1988 (unpublished).
19. A. QUARTERONI AND G. SACCHI-LANDRIANI, "Domain Decomposition Preconditioners for the Spectral Collocation Method," NASA CR-181620, 1988 (unpublished).
20. M. G. MACRAEG, C. L. STREETT, AND M. Y. HUSSAINI, "A Spectral Multi-Domain Technique Applied to High-Speed Chemically Reacting Flows," in *Proceedings, 2nd International Symposium on Domain Decomposition Methods, Los Angeles, CA* (January 1988).
21. M. R. MALIK, T. A. ZANG, AND M. Y. HUSSAINI, *J. Comput. Phys.* **61**, 64 (1985).
22. M. R. KHORRAMI, NASA Langley Research Center, Hampton, VA, private communications (1988).
23. L. M. MACK, *J. Fluid Mech.* **73**, 497 (1976).
24. M. R. MALIK, "COSAL—A Black Box Compressible Stability Analysis Code for Transition Prediction in Three-Dimensional Boundary Layers," NASA CR-165925, 1982 (unpublished).
25. A. ZEBIB, *J. Comput. Phys.* **53**, 443 (1984).
26. M. R. MALIK, "Prediction and Control of Transition in Hypersonic Boundary Layers," AIAA 19th Fluid Dynamics, Plasma Dynamics and Lasers Conference, Honolulu, Hawaii, June 8–10, 1987. AIAA Paper No. 87-1414, 1987 (unpublished).